Journal of Materials Chemistry C

ROYAL SOCIETY OF CHEMISTRY

PAPER

View Article Online
View Journal | View Issue

Cite this: J. Mater. Chem. C, 2021, 9, 9962

Temperature stable $Sm(Nb_{1-x}V_x)O_4$ ($0.0 \leq x \leq 0.9$) microwave dielectric ceramics with ultra-low dielectric loss for dielectric resonator antenna applications†

Fang-Fang Wu,[a] Di Zhou, *[a] Chao Du,[a] Shi-Kuan Sun,[b] Li-Xia Pang,[c] Biao-Bing Jin,[d] Ze-Ming Qi,[e] Jobin Varghese,[f] Qiang Li[g] and Xiu-Qun Zhang[h]

Herein, the structure and dielectric properties of $Sm(Nb_{1-x}V_x)O_4$ (SNV-x) ($0.0 \leq x \leq 0.9$) ceramics were studied by crystal structure refinement, Raman, transmission electron microscope (TEM), far-infrared/THz reflectivity spectroscopy and microwave dielectric tests. Three kinds of ultra-low dielectric loss and temperature-stable $Sm(Nb_{1-x}V_x)O_4$ ($0.2 \leq x \leq 0.4$) ceramics with permittivities of 18.01–16.89, $Q \times f$ values of 97 800–75 200 GHz (@ ~ 8.6 GHz), and TCF of −5.6 (x = 0.2), to +2.3 ppm $^{\circ}C^{-1}$ (x = 0.3), then −6.3 (x = 0.4) ppm $^{\circ}C^{-1}$ were synthesized in this system. It was found that V^{5+} substitution can reliably induce the phase transition of monoclinic fergusonite (M-fergusonite, $I2/a$) to tetragonal zircon phase (T-zircon, $I4_1/amd$) ($x \approx 0.3$), while effectively reducing the phase transition temperature. TEM shows that there were two different orientation domain structures in the M-fergusonite phase, and the widths of the two domain structures get closer with an increase in B-site substitution. Moreover, the variations in permittivity (ε_r), quality factor ($Q \times f$), and the temperature coefficient of resonance frequency (TCF) were strongly related to the crystal distortion and phase transition. Notably, a rectangular dielectric resonator antenna (RDRA) was fabricated with an $Sm(Nb_{0.8}V_{0.2})O_4$ (SNV-0.2) specimen. The antenna resonated at 27.04 GHz and had a bandwidth of ~820 MHz (S11 < −10 dB). This system is a good candidate for 5G and future millimeter-wave applications.

Received 24th May 2021,
Accepted 30th June 2021

DOI: 10.1039/d1tc02390j

rsc.li/materials-c

Introduction

Multiple-input multiple-output (MIMO) and massive MIMO technology remain promising for 5G and millimeter-wave antennae with ultra-high channel capacity. Therefore, as an important part of MIMO technology, antenna elements have always been an area of concern for researchers.[1–6] Compared with traditional antennas, DRA has gradually become the focus of scholarly research owing to its advantages of design flexibility, large bandwidth, non-appearance of metallic losses, high gain, versatile shapes and versatile radiation characteristics.[7–9] Moreover, research has been carried out on DRA-MIMO for 5G.[8] DRA is a resonant antenna consisting of low loss microwave dielectric materials (MWDCs); hence, dielectric materials with low relative permittivity (ε_r) for reduction of signal delay, a high $Q \times f$ for frequency selectivity, and a near-zero temperature coefficient of resonant frequency (TCF) for thermal stability are desirable to meet the specifications of 5G/6G. Currently, microwave dielectric ceramics that satisfy these properties simultaneously are scarce and/or not suitable for 5G and the millimeter-wave band, which

[a] Key Laboratory of Multifunctional Materials and Structures, Ministry of Education, School of Electronic Science and Engineering, Xi'an Jiaotong University, Xi'an 710049, Shaanxi, China. E-mail: zhoudi1220@gmail.com
[b] School of Material Science and Energy Engineering, Foshan University, Foshan, Guangdong, 528000, P. R. China
[c] Micro-optoelectronic Systems Laboratories, Xi'an Technological University, Xi'an 710032, Shaanxi, China
[d] Research Institute of Superconductor Electronics (RISE), School of Electronic Science and Engineering, Nanjing University, Nanjing, Jiangsu, 210093, China
[e] National Synchrotron Radiation Laboratory, University of Science and Technology of China, Hefei, China
[f] Hybrid Microsystems, Fraunhofer Institute for Ceramic Technology and Systems IKTS, Winterbergstr 28, 01277 Dresden, Germany
[g] ZTE Corporation, District Nanshan, Shenzhen, 518000, China
[h] ZTE Corporation, District Yuhuatai, Nanjing, 210012, China

† Electronic supplementary information (ESI) available: Reagents and the synthesis of SNV-x ($0 \leq x \leq 0.9$) and characterization test, Microwave dielectric properties of $ReNbO_4$-based (Re = La, Nd, Sm) compounds (Table S1), room-temperature crystal structure of $Re(Nb_{1-x}V_x)O_4$ (Re = La, Ce, Nd) compounds (Table S2), refined lattice parameters of the SNV-x ($0 \leq x \leq 0.4$) ceramics (Tables S3 and S4), SEM images of the SNV-x ($0 \leq x \leq 0.2$) and BSEI of polished surface of the SNV-x ($0.3 \leq x \leq 0.7$) ceramics (Fig. S4), The phonon parameters obtained by fitting the infrared reflection spectrum of the SNV-x ($0.2 \leq x \leq 0.4$) ceramics (Table S6). See DOI: 10.1039/d1tc02390j

is the driving force promoting the continuous research and development of MWDCs in this field.

Rare-earth niobates ($ReNbO_4$, Re = La to Lu, Y) have been extensively investigated in the fields of phosphors, fuel cells and photocatalysis.[10–12] It is well known that $ReNbO_4$ have a similar structure and experience a second-order and reversible ferroelastic phase transition to tetragonal scheelite (T-scheelite, $I4_1/a$) at high temperature and to monoclinally distorted monoclinic fergusonite (M-fergusonite, $I2/a$) at low temperature (Fig. 1). The radii of both rare earth ions and cations at the B-site have an influence on the phase transition temperature, which increases with a decrease in the size of the rare-earth ions.[13–15] In 2006, Kim found that a serial permittivity (16–20) is first of all an advantage of $ReNbO_4$ ceramics for microwave application, and the phase transformation is a dominant factor in ε_r and TCF.[16] Hence, the excellent microwave dielectric properties of $ReNbO_4$ (Re = La, Nd and Sm) are research hotspots in the field of functional ceramics (Table S1, ESI†).[17–34] To summarize, B-site substitution is an effective way to induce phase transition in $ReNbO_4$ ceramics, to an extent optimizing the microwave dielectric properties. However, meeting the dielectric properties of low permittivity, high $Q \times f$ and near-zero TCF synchronously is difficult because of their entanglement. In short, the results obtained (Table S1, ESI†) could not fulfil the utilization of the microwave ceramics in millimeter-wave communication very well. In addition, there are few investigations on $SmNbO_4$ ceramics with a higher phase transition temperature ($\sim$860 °C),[16] which are expected to be candidates for 5G and future millimeter-wave bands because of their relatively remarkable microwave dielectric properties ($\varepsilon_r \sim 18.8$, $Q \times f \sim 56\,300$ GHz and TCF ~ -40 ppm °C^{-1}).[16]

Scientists studied the phase evolution and lattice constants of Nb^{5+} ($R_{Nb}{}^{5+}$ = 0.64 Å, CN = 6) in $ReNbO_4$ (Re = La, Ce, Nd) substituted by the smaller V^{5+} ($R_V{}^{5+}$ = 0.54 Å, CN = 6) ion, and explained them with Landau theory.[35] It can be concluded that there is a phase transition of M-fergusonite to T-scheelite, and the region of T-scheelite structure narrowed and even disappeared at room temperature with an increase in V^{5+} content for heavier rare-earths (smaller radius ions).[35,36] It is reported that the phase transformation will be promising for nearly zero TCF values, while adjusting the permittivity.[16] Furthermore, compared with Nb^{5+} (ionic polarizability: 3.97 Å^3), V^{5+} has a smaller ionic polarizability (2.92 Å^3), which can reduce the dielectric constant estimated by polarizability and the Clausius–Mosotti relation,[37,38] applying $SmNbO_4$ ceramics in 5G and millimeter-wave applications. More importantly, the structure and microwave dielectric properties of the Nb-site substituted by V^{5+} in an $SmNbO_4$ compound have not yet been reported.

In this paper, the phase structure, microstructure, densification and microwave dielectric properties of SNV-x ($0.0 \leq x \leq 0.9$) ceramics were studied in detail. In addition, the SNV-0.2 ceramic material was designed into an RDRA with aperture coupling feeding configuration excitation by the time domain finite element simulation software CST Microwave Studio 2019®. The corresponding prototype RDRA was fabricated, and the performance of the antenna was tested.

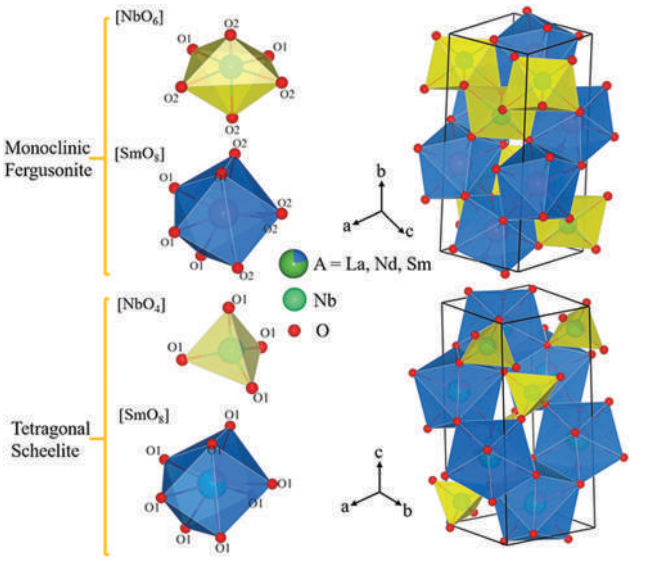

Fig. 1 Schematic diagrams to illustrate the crystal structure of $ReNbO_4$.

Results and discussion

It was observed that pure $SmNbO_4$ (SN) was well formed at 1480 °C and crystallized in an M-fergusonite ($I2/a$) structure in Fig. 2a, which is similar to the results in the literature.[33,39] With an increase in V^{5+} doping, two phase regions can be detected: M-fergusonite (JCPDS #22-1303) within the range of $0 \leq x < 0.3$, and the coexistence of M-phase and T-zircon in the range of $0.3 \leq x \leq 0.9$. This can be ascribed to the smaller ionic radius of V^{5+} (0.54 Å, CN = 6) than Nb^{5+} (0.64 Å, CN = 6).[40] Moreover, the diffraction peaks (200) and (112) of the T-zircon phase $SmVO_4$ (SV) are observed at x = 0.3 and become stronger with an increase in x; meanwhile the peaks ($\bar{1}21$) and (031) of M-fergusonite converge and become weaker and broader, suggesting that the $[NbO_6]$ octahedra make a transition to $[NbO_4]$ tetrahedra. Whereas, there is no T-scheelite structure in SNV-x ceramics at room temperature, unlike the $Re(Nb_{1-x}V_x)O_4$ (Re = La, Ce, Nd) series (Table S2, ESI†). This proves the prediction of a direct transition of M-fergusonite to the T-zircon phase without a T-scheelite phase with heavier Sm^{3+} ions (Sm > Nd > Ce > La) at the A-site.[35] Discontinuity of the thermal expansion curve (Fig. 2b) is observed in a thermal expansion experiment because of the monoclinic–tetragonal phase transition. The thermal expansion coefficient (a_L) of the V^{5+} doping component is larger than that of undoped SN (in the inset to Fig. 2b). The temperature of onset shrinkage (T_c) decreases from 800 °C (SN) to 405 °C (SNV-0.2) with the higher V^{5+} content, which is contrary to the substitution at the A-site of other rare-earth cations.[16,33] Rooksby reported that variation in the interatomic bonding forces in the $[NbO_4]$ and $[TaO_4]$ tetrahedron with the same rare-earth ions was responsible for the difference in the phase transition temperature. Ta–O bonds have greater interatomic bonding forces than Nb–O bonds in these samples. Hence, tantalates need more energy

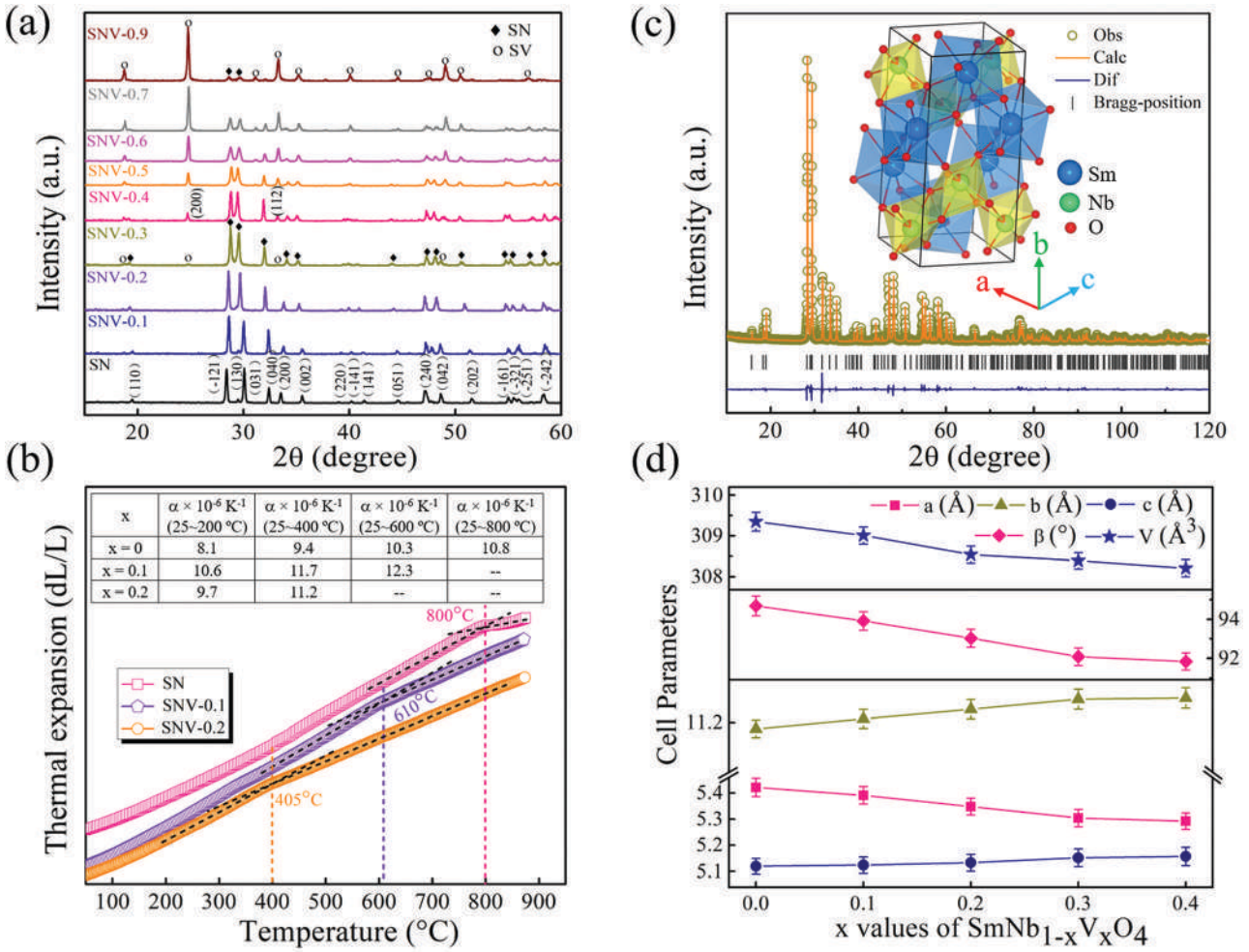

Fig. 2 (a) X-ray diffraction patterns of $Sm(Nb_{1-x}V_x)O_4$ ($0 \le x \le 0.9$) ceramics sintered at optimal temperatures. (b) Thermal expansion data of $Sm(Nb_{1-x}V_x)O_4$ ($0 \le x \le 0.2$) as a function of temperature. (c) Rietveld refinement plot of $Sm(Nb_{0.8}V_{0.2})O_4$ ceramic; all the results give satisfactory refinement parameters (R_{wp}, R_p, χ^2). (d) Lattice parameter data of $Sm(Nb_{1-x}V_x)O_4$ ($0 \le x \le 0.4$) ceramics as a function of x.

to eliminate monoclinic distortion.[15] In this paper, the bond length of Nb/V–O increases with doping of V^{5+} (Table S4, ESI†), leading to a decrease in interatomic bond forces. This makes it easier to eliminate monoclinic distortion by supplying less thermal energy than to undoped, resulting in a decrease in the phase transition temperature. Moreover, compared with T-zircon, M-fergusonite has a larger a_L, resulting in the thermal expansion slowing suddenly with higher temperature ($>T_c$), similar to $LaNbO_4$. To investigate the details of the crystal structure of SNV-x ($0.1 \le x \le 0.4$) ceramics, refinements were performed. These confirmed that there are two phase regions, as discussed above. The structure consists of distorted $[SmO_8]$ dodecahedrons and $[NbO_6]$ octahedrons in M-fergusonite. $[NbO_6]$ octahedrons were connected by sharing an edge, and the $[SmO_8]$ units were placed in the propagating chains of $[NbO_6]$ sharing the oxygen (in the inset to Fig. 2c). With this special structure, the microwave dielectric properties are very sensitive to the distortion of $[NbO_6]$. It was found that the atomic interactions changed as the amount of V^{5+} increased, which transforms the bond length of the $[NbO_6]$ octahedron, and may affect the microwave dielectric properties of the ceramics (Tables S3 and S4, ESI†). In the range of $0 \le x < 0.3$, the lattice parameters of b and c increase linearly with the increase in V^{5+} content, while a and β decrease, as shown in Fig. 2d. All these changes indicate that the transition can be regarded as equivalent to eliminating the monoclinic distortion of the tetragonal structure, resulting in the continuous phase transition of M-fergusonite to the T-zircon phase. The unit cell volume shrinks from 309.35 Å^3 to 308.21 Å^3 in M-fergusonite with the increase in V^{5+}, which agrees with the conclusion that there is a contraction of the cell volume with increases in the tetragonal structure for the $Re(Nb_{1-x}V_x)O_4$ (Re = La, Ce, Nd) series.[35]

To explore the micrograph and crystal structure, HRTEM microstructure and SAED patterns were performed. There are two possible deformation modes of the unit cell because of the four-fold symmetry of the prototypic phase for M-fergusonite. Therefore, it is found that the M-fergusonite structure has two different orientation domain (I and II) structures,[41–44] which is proved by the two sets of diffraction spots, as shown in Fig. 3a, b and d. The widths of the two domain structures get closer

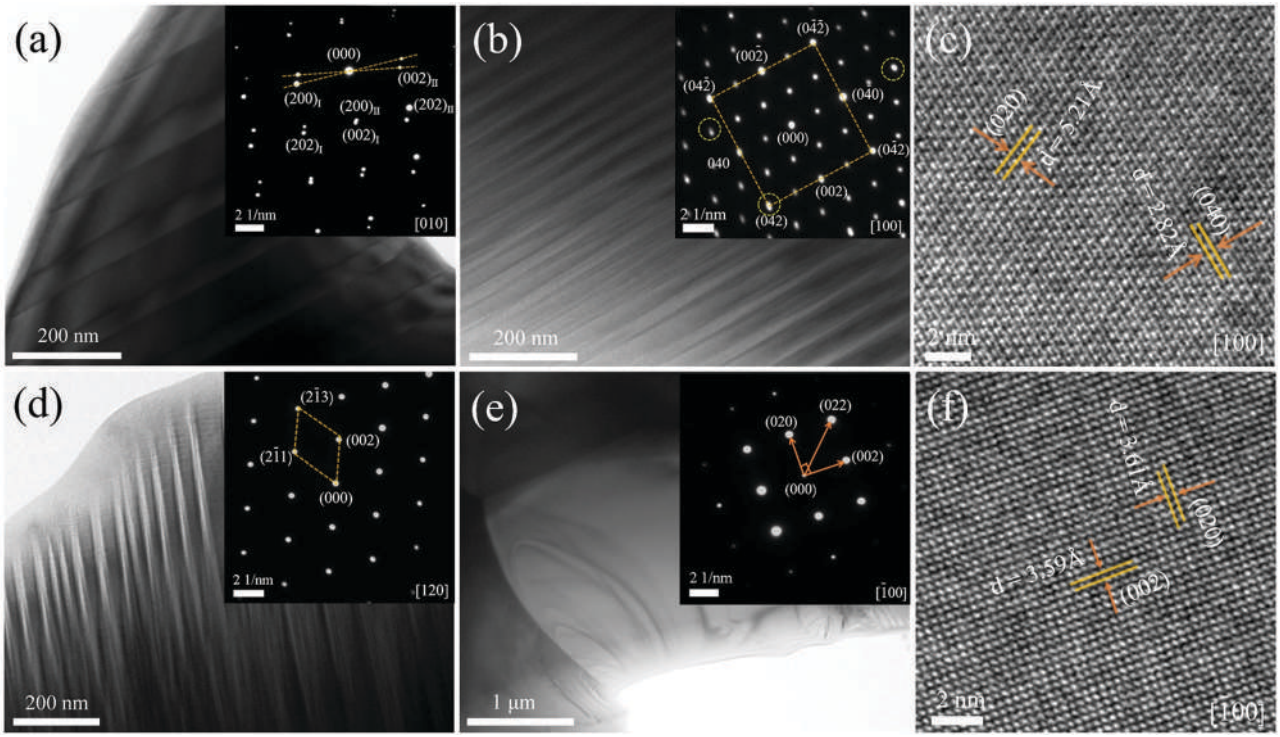

Fig. 3 SAED and microstructure of the monoclinic fergusonite phase of $Sm(Nb_{1-x}V_x)O_4$ ($0 \leq x \leq 0.3$) ceramics: (a) $SmNbO_4$, (b) $Sm(Nb_{0.8}V_{0.2})O_4$, and (d) $Sm(Nb_{0.7}V_{0.3})O_4$ taken along the [010], [100] and [120] zone axes at room temperature, respectively. (e) SAED and microstructure of tetragonal zircon phase $SmVO_4$ in the $Sm(Nb_{0.7}V_{0.3})O_4$ component taken along the [$\bar{1}$00] zone axes. (c and f) HRTEM images of monoclinic fergusonite $Sm(Nb_{0.8}V_{0.2})O_4$ and tetragonal zircon phase $SmVO_4$, respectively.

with the increase in B-site substitution. Each set of spots corresponds to one of the two orientations. Furthermore, the two sets of diffraction spots approach each other as x increases, which is consistent with the variation in width of the domain structures and the convergence of the XRD diffraction peaks ($\bar{1}21$) and (031), respectively. The zone axis for both sets of spots in SNV-x (x = 0, 0.2, 0.3) specimens are [010], [100] and [120], respectively. In the $Sm(Nb_{0.7}V_{0.3})O_4$ (SNV-0.3) component, a tetragonal phase is observed taken along the [$\bar{1}$00] zone axis apart from the monoclinic phase, which proved to be the T-zircon phase SV, as shown in Fig. 3e. According to the HRTEM images, the lattice fringes in the particle match well with the interplanar spacing of the monoclinic and tetragonal structures in Fig. 3c and f, respectively.

The results of SEM micrographs and backscattered scanning electron images (BSEI) of SNV-x ($0.0 \leq x \leq 0.9$) specimens sintered at the densification temperature for 3 hours are shown in Fig. S4 (ESI†). This shows that homogeneous, relatively flat surfaced and micro-pored ceramics are obtained. Furthermore, the optimal sintering temperature and mean size of the samples are reduced from 1480 °C (SN) to 1150 °C (SNV-0.9) and 4.93 μm to 1.92 μm with the increase in x (melting point of V_2O_5 is 690 °C $\leq$ 1485 °C for Nb_2O_5), respectively. This indicates that the increase in V^{5+} ions reduces both the sintering temperature and the grain size. In addition, the BSEI images display two different types of particles in white and gray, respectively, as shown in Fig. 4. EDS analysis of $Sm(Nb_{0.6}V_{0.4})O_4$ (SNV-0.4) ceramic in the dashed area shows that the white and gray areas are rich in niobium (M-fergusonite) and vanadium (T-zircon), respectively, which is consistent with the results of the XRD analysis above.

Group theory predicts that there are 18 Raman active modes ($8A_g + 10B_g$) possible for the M-fergusonite structure ($I2/a$), which was proved by Siqueira *et al.*[45] However, 13 vibrational modes were identified because the space group symmetry deviates only slightly from a much higher space group symmetry,[39] as illustrated in Fig. 5a. Referring to reports the vibrational modes of [NbO_6] at high wavenumber band are due to the covalent nature of the Nb–O bonds. Frequencies below 300 cm^{-1} are assigned to external vibrations.[33,46,47] There is no obvious shift in the Raman modes of the SNV-x ceramics in the range of $0 \leq x < 0.3$; nevertheless the full widths at half maximum of the strong Raman modes (810.3, 332.1 cm^{-1}) increase because the B-site substitution affects the rigidity of the [NbO_6] octahedron. A new Raman active mode is observed around 878.9 cm^{-1} at SNV-0.3 and becomes stronger with increasing x. Based on the XRD and SEM analysis above, it belongs to the symmetric stretching V–O vibrations ($A_{1g}(\nu_1)$) of SV. Meanwhile, two anti-symmetric stretching V–O vibrations $B_{1g}(\nu_3)$ and $E_g(\nu_3)$ appear at nearly 810 cm^{-1}, in which the $E_g(\nu_3)$ mode overlaps with the symmetric Nb–O vibrations (A_g at 810 cm^{-1}), as shown in Fig. 5b. With the increase in V^{5+}, the anti-symmetric Nb–O vibration of SN between ~330 and 700 cm^{-1} weakens and even disappears, whereas the V–O vibration $B_{1g}(\nu_4)$ and $A_{1g}(\nu_2)$ modes of SV at 477.4 and 378.4 cm^{-1} are stronger, and the Raman modes of SNV-0.9 belong completely to the T-zircon structure.[48,49]

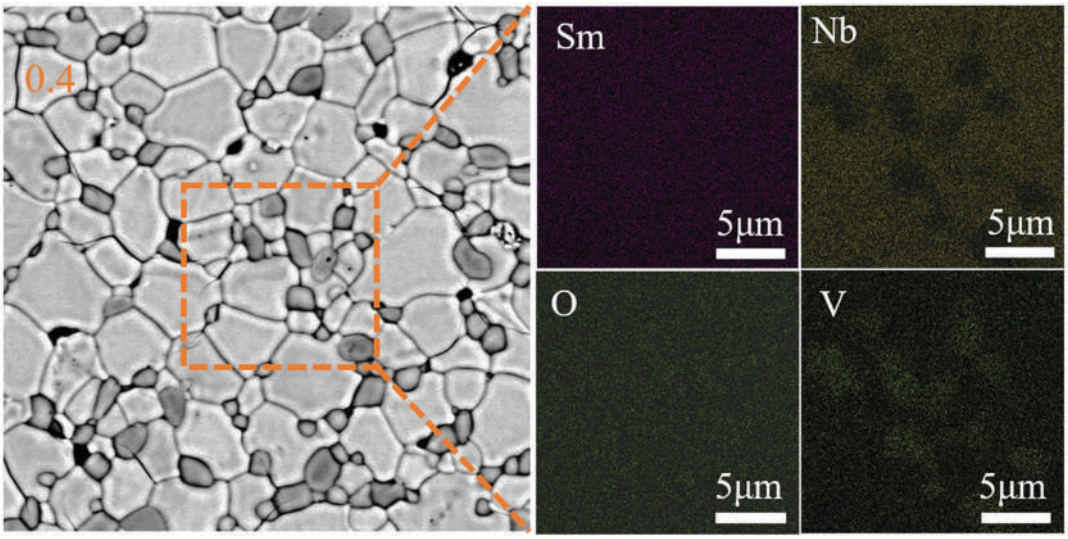

Fig. 4 The associated energy-dispersive analysis (EDS) on surfaces of the $Sm(Nb_{0.6}V_{0.4})O_4$ ceramics sintered at optimal temperatures.

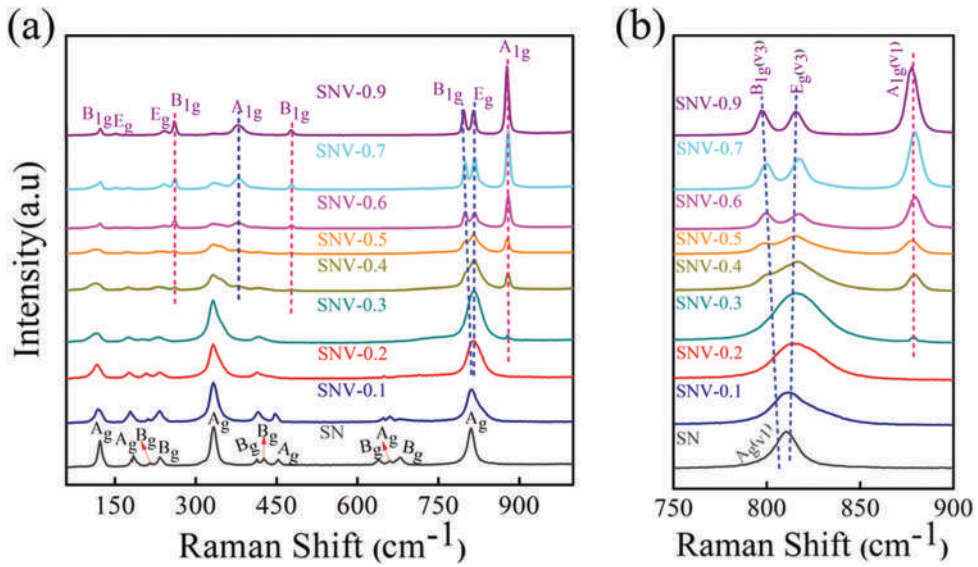

Fig. 5 (a) Room-temperature Raman spectra of $Sm(Nb_{1-x}V_x)O_4$ ($0 \le x \le 0.9$) ceramics (ν_1, ν_2, ν_3, and ν_4 corresponding to symmetric stretch, symmetric bending, antisymmetric stretch, and antisymmetric bending, respectively). (b) Raman spectra in the range of 750–900 cm^{-1}.

In addition, the intensities of SNV-0.9 at low wavenumber are weaker than that of SN, which may be determined by the presence of multiple cations at the B-site.[33] The Raman spectra of SNV-x ($0 \le x \le 0.9$) further show that the substitution of V^{5+} ions leads to the transformation of M-fergusonite to T-zircon instead of the T-scheelite structure.

Fig. 6 shows the permittivity (ε_r), quality factor ($Q \times f$), and temperature coefficient of the resonant frequency (TCF) values of the SNV-x ceramics. The permittivity of ceramics depends on their intrinsic parameters (polarizability and structural characteristics) and extrinsic parameters (porosity and secondary phase).[50,51] With an increase in V^{5+} content, ε_r increases from 16.5 (SN) to 18.1 (SNV-0.1), and then decreases to 11.6 (SNV-0.9). The slope of the decrease at $0.1 \le x < 0.3$ is less than that of $0.3 \le x < 0.9$, as shown in Fig. 6a. The secondary phase SV ($\varepsilon_r \sim 11.70$) should be responsible for this phenomenon.[52] Moreover, the influence of porosity on the permittivity could be ignored in SNV-x ($0.1 \le x \le 0.4$) ceramics with the high relative density (>96.5%) shown in Fig. 6e. Meanwhile, the measured ε_r retains a similar tendency to the calculated value but for SN, both of them reduce as x increases, as shown in Fig. 6d. In other words, the change in ε_r can be explained well by the estimated polarizability and the Clausius–Mosotti relation.[37,38]

$$a_x = a_{Sm^{3+}} + (1 - x)a_{Nb^{5+}} + xa_{V^{5+}} + 4a_{O^{2-}} \quad (1)$$

$$\varepsilon_S = \frac{3V_m + 8\pi a_x}{3V_m - 4\pi a_x} \quad (2)$$

where $\alpha_{Sm}{}^{3+}$, $\alpha_{Nb}{}^{5+}$, $\alpha_V{}^{5+}$, $\alpha_O{}^{2-}$ and V_m are the polarizabilities of Sm^{3+}, Nb^{5+}, V^{5+}, O^{2-} and the molecular molar volume, respectively. It had

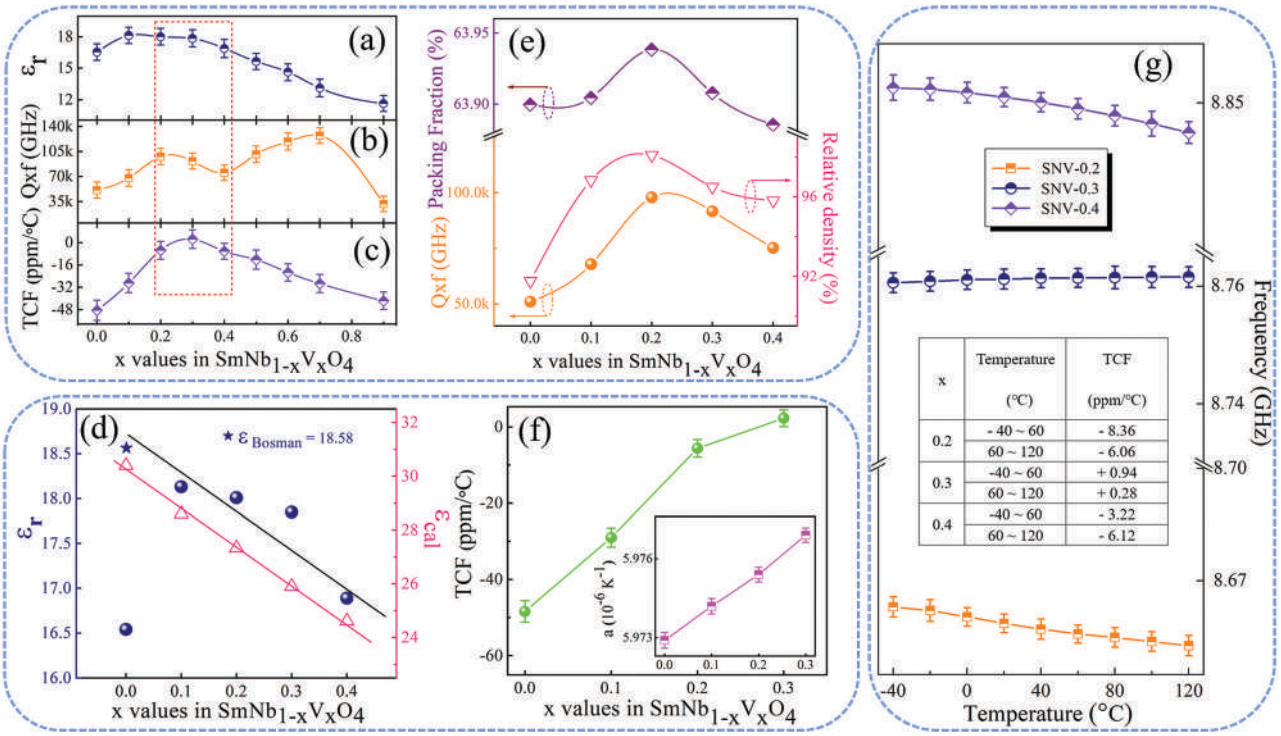

Fig. 6 The bulk microwave dielectric properties of permittivity ε_r (a and d), $Q \times f$ values (b and e) and TCF values (c and f) of the $Sm(Nb_{1-x}V_x)O_4$ ceramics as a function of x value. (g) The TCF values of $Sm(Nb_{1-x}V_x)O_4$ ($0.2 \leq x \leq 0.4$) as a function of temperature.

been reported that the ionic polarizability of V^{5+} (2.92 Å^3) is smaller than that of Nb^{5+} (3.97 Å^3),[38] which is consistent with the current conclusion. Therefore, the lower polarizability of the V^{5+} (2.92 Å^3) ions is responsible for the decrease in permittivity. The measured ε_r (16–20) are smaller than the calculated values (24–31), and the deviation between them is caused by distortion of the M-fergusonite structure.[16] The micro-pores in the SEM image (Fig. S4, ESI†) and the low relative density (~91.8%) (Fig. 6e) indicate the higher porosity of the SN ceramic, resulting in the lower measured ε_r. The modified value is 18.5 (the asterisk in Fig. 6d) by applying Bosman and Havinga's correction,[37,53] which is close to the measured result obtained by Kim.[16] Clearly the $Q \times f$ values show a double parabolic distribution in Fig. 6b, and the two maximum values are 97 800 GHz (f = 8.64 GHz, x = 0.2) and 127 100 GHz (f = 9.59 GHz, x = 0.7), respectively. The irregular behavior is related to the structural deformation induced by substitution of V^{5+} ions, and reported in $La(Nb_{1-x}V_x)O_4$ ceramics.[28] It was reported that the structural deformation could be evaluated with the packing fraction.[54,55] For the M-fergusonite structure of $Sm(Nb_{1-x}V_x)O_4$ ceramics, the packing fraction is defined as eqn (3):

$$\text{Packing fraction} = \frac{3\pi/4 \times \left(r_{Sm}{}^3 + r_{(Nb/V)}{}^3 + 4r_O{}^3\right)}{V_{cell}} \times 4 \quad (3)$$

where r_{Sm}, $r_{(Nb/V)}$, and r_O are the effective ionic radii at each coordination number, and V_{cell} is the unit cell volume obtained by refinement. The dependence of the $Q \times f$ values on the relative density and packing fraction are clearly confirmed in Fig. 6e. The variation in the $Q \times f$ in SNV-x (x = 0.1–0.4) ceramics is similar to the relative density and packing fraction, increasing first and then decreasing with the increase in V^{5+} substitution for Nb^{5+}. Accordingly, the lattice vibration decreases with an increase in packing fraction, thereby reducing the intrinsic loss. For the SN ceramic, more pores would be introduced in the preparation process to lower the relative density, resulting in a poor $Q \times f$ value. The TCF ranging from −48.8 (SN) to +2.3 ppm °C^{-1} (SNV-0.3) shows an almost monotonous increase, and then decreases to −41.7 ppm °C^{-1} (SNV-0.9) in Fig. 6c, which is dominated by the crystal distortion and phase transition.[28] TCF is a function of the temperature coefficient of ε_r (τ_ε) and the linear thermal expansion coefficient (a_L).

$$\text{TCF} = -\left(\frac{\tau_\varepsilon}{2} + a_L\right) \quad (4)$$

In this work, the TCF values are closely related to a_L, both of them increasing with an increase in V^{5+} doping in the range of $0 \leq x \leq 0.3$, as shown in Fig. 6f. Similar phenomena exist in other solid solution ceramic systems, like $Nd(Nb_{1-x}Sb_x)O_4$, $NdNbO_4$–xAl_2O_3, $La(Nb_{1-x}V_x)O_4$ *etc.*[28,56,57] However, a_L is not the only factor affecting TCF, which can be adjusted by controlling the phase transformation temperature in an SNV system [16]. In this paper, the phase transformation temperature of the ceramics is reduced by V^{5+} substitution (Fig. 2b), and the TCF value changes from negative to positive (Fig. 6c). Here, the TCF values were measured in ranges from 25 to 85 °C and −40 to 120 °C, respectively, to provide more information for future applications. The resonant frequencies of the three

Table 1 Microwave dielectric properties of the $Sm(Nb_{1-x}V_x)O_4$ ($0.2 \le x \le 0.4$) ceramics

x	ε_r	$Q \times f$/GHz	TCF/(ppm °C^{-1}) 25–85 °C
0.2	18.01	97 800	−5.6
0.3	17.85	91 500	+2.3
0.4	16.89	75 200	−6.3

ceramics (SNV-0.2, SNV-0.3 and SNV-0.4) change little as the temperature increases, and near-zero TCF values can be obtained (Fig. 6c and g), showing excellent temperature stability. Notably, this is an effective method to adjust near-zero TCF by the substitution of V^{5+} for Nb^{5+} in $ReNbO_4$ ceramics. The excellent performances of the SNV-x (x = 0.2, 0.3 and 0.4) specimens are summarized in Table 1.

Far Infrared (FIR) reflectivity spectroscopy is a useful approach to describe the relationship between lattice vibrations and intrinsic dielectric properties. To further research the intrinsic microwave dielectric properties of SNV-x ($0 \le x \le 0.9$) ceramics, the infrared reflectance spectra were analyzed.

$$\varepsilon \times (\omega) - \varepsilon(\infty) = \sum_{j=1}^{n} \frac{(z_j e)^2 / m_j V_j \varepsilon_0}{\omega_{T_j}{}^2 - \omega^2 - j\gamma_j \omega} \quad (5)$$

The relevant parameters in eqn (5) were described in previous work.[58] The relationship between complex reflectivity permittivity and $R(\omega)$ can be expressed as eqn (6).

$$R(\omega) = \left| \frac{1 - \sqrt{\varepsilon^*(\omega)}}{1 + \sqrt{\varepsilon^*(\omega)}} \right|^2 \quad (6)$$

All the infrared reflection spectra of SNV-x ($0.0 \le x \le 0.9$) ceramics can be well fitted by employing eqn (5) and (6) with fourteen modes (Fig. 7a–d). The relevant phonon parameters of SNV-x ($0.2 \le x \le 0.4$) ceramics as representative data are shown in Table S6 (ESI†). The calculated permittivity values for SNV-0.2, SNV-0.3 and SNV-0.4 ceramics are 20.24, 13.10 and

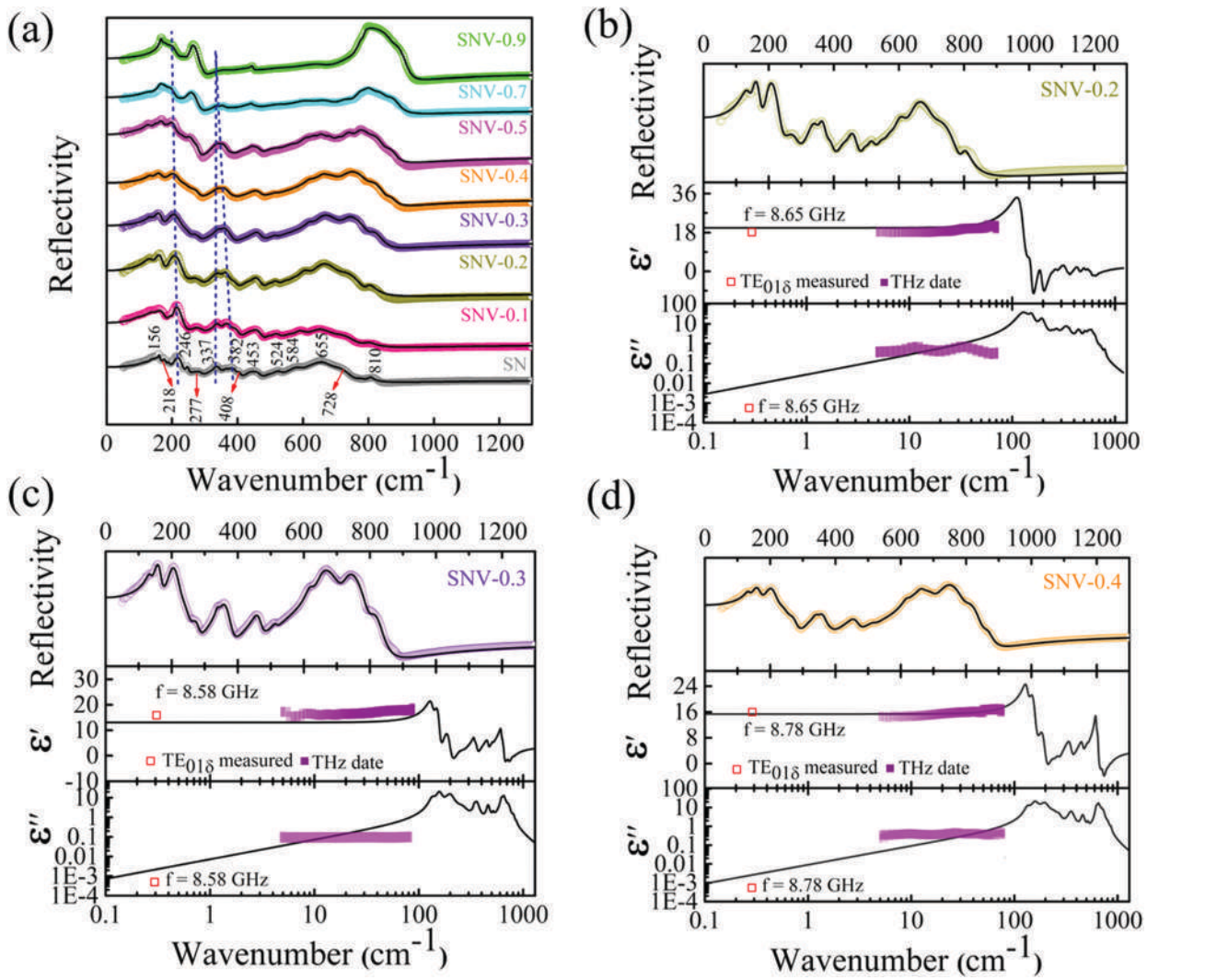

Fig. 7 (a) Experimental and fitted infrared reflection spectra (solid line for fitted and dotted for experimental) of $Sm(Nb_{1-x}V_x)O_4$ ($0.0 \le x \le 0.9$) ceramics. The fitted complex dielectric spectrum and THz spectra of (b) $Sm(Nb_{0.8}V_{0.2})O_4$, (c) $Sm(Nb_{0.7}V_{0.3})O_4$ and (d) $Sm(Nb_{0.6}V_{0.4})O_4$ ceramics (the squares are the measured values in the microwave band).

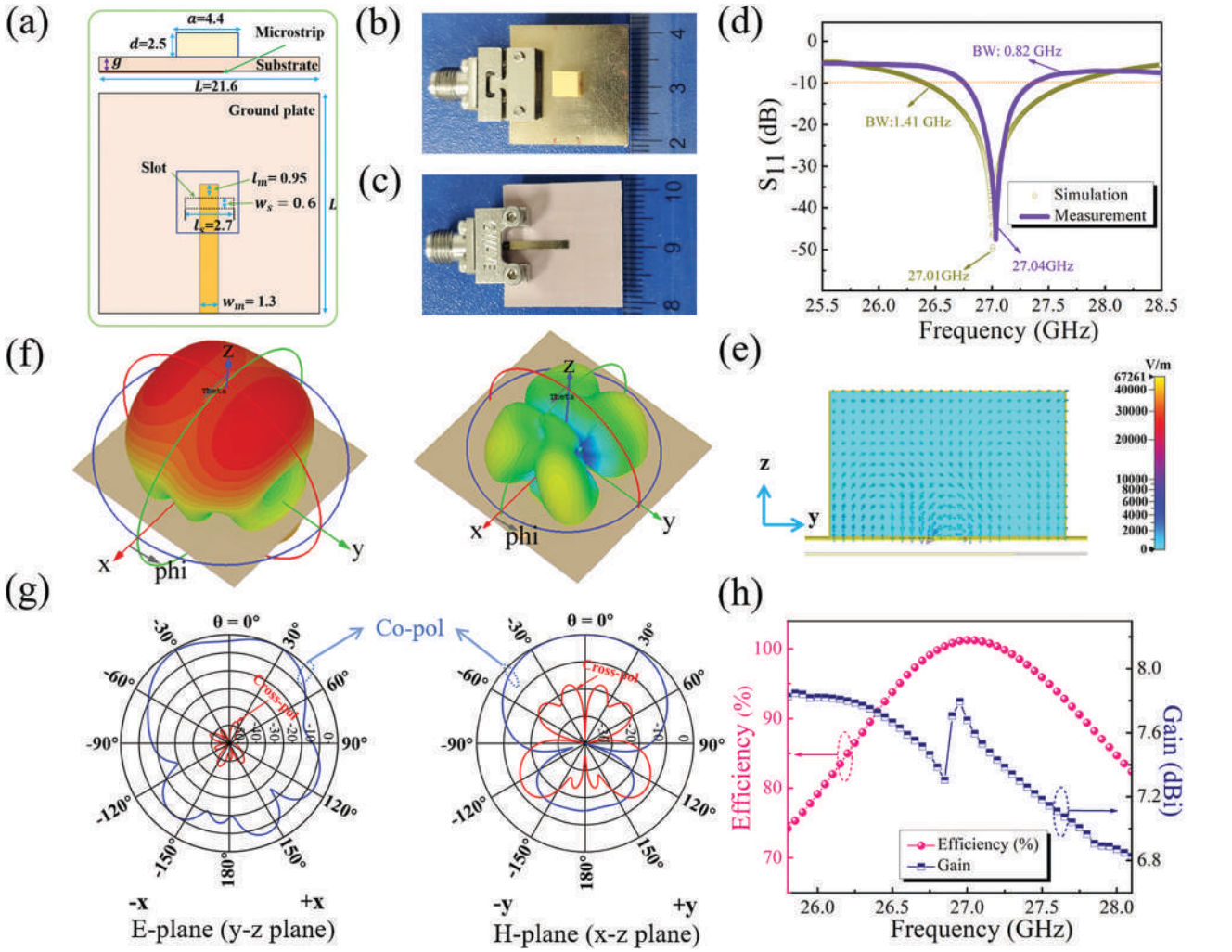

Fig. 8 The geometries (unit: millimeter) of (a), top (b) and bottom (c) views for the rectangular fabricated dielectric resonator antenna. (d) The simulated and measured return loss (S11) of the proposed antenna. The simulation results of (e) electric field and (f) simulated radiation pattern of the co-polarized and cross-polarized of the antenna at 27.01 GHz. (g) Simulated normalized radiation patterns at phi = 0° and phi = 90°. (h) Simulated antenna radiation efficiencies and gains of the rectangular dielectric resonator antenna.

15.37, respectively. In addition, the experimental results coincide with the calculated dielectric constant and loss, which indicates that phonon absorption in the infrared region is the main reason for the dielectric polarization. Moreover, the real part (ε') of the permittivity obtained with the THz (0.2–2 THz) results shows a consistent trend with the fitted result of the FIR reflectivity spectra, whereas the imaginary part (ε''), is inversely proportional to the Q value, fluctuating slightly in the millimeter-wave frequency range and is still acceptable. This means that the three kinds of materials mentioned above are good candidates for 5G and future millimeter-wave applications.

With the rapid development of wireless communication systems, antennae, as a key component, have attracted more and more attention. Therefore, we used the ceramic (SNV-0.2) with excellent microwave dielectric properties ($\varepsilon_r \sim 18.01$, $Q \times f \sim 97\,800$ GHz, TCF ~ -5.6 ppm $^{\circ}C^{-1}$) to produce an applicable RDRA. In this article, using aperture coupling feeding configuration excitation and dimensions of $a = 4.4$ mm, $b = 4.4$ mm, and $h = 2.5$ mm, an RDRA was designed, which gave excellent radiant performances. Fig. 8a–c show a schematic diagram of the designed RDRA and the real RDRA, respectively. As presented in Fig. 8d, the simulated center frequency and bandwidth with 27.01 GHz and 1410 MHz ($S11 < -10$ dB) were offered by the antenna, respectively, and the measured results were 27.04 GHz and 820 MHz, respectively. That is, the center frequencies for the simulated and measured data are basically the same, but the measured bandwidth is less than the simulated one. The physical mechanism of the designed RDRA is revealed by an investigation into the electric field distribution at 27.01 GHz. The displacement current in the RDRA belongs to the $TE_{\delta 31}$ higher modes,[59] with a peak in the broadside direction (along the z-axis), as shown in Fig. 8e. The longitudinal direction of the electric-field in the direction of electromagnetic wave propagation is not zero, and the magnetic-field is zero. Fig. 8f and g show the simulated radiation patterns of the designed RDRA.

The result is predictable for the RDRA when supplied with a knowledge of the modes. For both phi = 0° and phi = 90° patterns, the co-polarization field is approximately over 20 dB stronger than the cross-polarization field in the direction of θ = 0°. The radiation efficiency is greater than 91.2% in the bandwidth range, and the gain is 7.79 dBi near the resonant frequency, as shown in Fig. 8h. In addition, the higher gains compared with a slot antenna implies that the resonance is caused by the ceramic RDRA rather than the feed slot.

Conclusion

The phase evolution, microstructure, phase transition temperature and microwave dielectric properties of SNV-x ($0 \leq x \leq 0.9$) ceramics were intensively researched. V^{5+} substitution for Nb^{5+} can reliably induce the phase transition of M-fergusonite to T-zircon ($x \approx 0.3$). The M-fergusonite phase has two different orientations of the domain structure, and the widths of the two domain structures get closer with an increase in V^{5+} substitution. Furthermore, the phase transition temperature, permittivity (ε_r), $Q \times f$ and the TCF values can be regulated by controlling the V^{5+} content. From the far-infrared and THz, it is concluded that the main polarization originates from ionic polarization rather than electron polarization, and both the values of ε_r and $Q \times f$ are determined by phonon absorption in the microwave region. Remarkably, three kinds of ultra-low dielectric loss and temperature-stable SNV-x (x =0.2, 0.3, 0.4) ceramics with permittivities of 18.01–16.89, $Q \times f$ values of 97 800–75 200 GHz (@ ~ 8.6 GHz), and TCF of −5.6 ppm $°C^{-1}$ (SNV-0.2) to +2.3 ppm $°C^{-1}$ (SNV-0.3), then −6.3 ppm $°C^{-1}$ (SNV-0.4) are obtained. An RDRA device fabricated with SNV-0.2 ceramic exhibits good performances, and resonated at 27.04 GHz with a bandwidth of 820 MHz ($S_{11} < -10$ dB). It is a potential candidate for 5G and future millimeter-wave applications.

Conflicts of interest

The authors declare no competing financial interest.

Acknowledgements

This work was supported by the National Key Research and Development Program of China (Grant 2017YFB0406301), the National Natural Science Foundation of China (51972260, 52072295), the Fundamental Research Funds for the Central University (No. xzy022020046), and the 111 Project of China (B14040). The SEM and TEM works were done at the International Center for Dielectric Research (ICDR), Xi'an Jiaotong University, Xi'an, China and the authors thank Ms Y. Z. Dai and Mr S. D. Cheng for their help in using SEM and TEM. The authors thank the administrators in IR beamline workstation (BL01B) of National Synchrotron Radiation Laboratory (NSRL) for their help in the IR measurement and fitting.

Notes and references

1 Y. Zhan and L. Li, *J. Alloys Compd.*, 2021, **857**, 157608–157618.
2 K. L. Wong, C. Y. Tsai and J. Y. Lu, *IEEE Trans. Antennas Propag.*, 2017, **65**, 1765–1778.
3 Z. J. Qin, G. Y. Wen, M. Zhang and J. Wang, *Electron. Lett.*, 2016, **52**, 416–418.
4 M. M. Kamal, S. Y. Yang, S. H. Kiani, D. A. Sehrai, M. Alibakhshikenari, M. Abdullah, F. Falcone, E. Limiti and M. Munir, *Electronics*, 2021, **10**, 673–682.
5 H. H. Guo, M. S. Fu, D. Zhou, C. Du, P. J. Wang, L. X. Pang, W. F. Liu, A. S. B. Sombra and J. Z. Su, *ACS Appl. Mater. Interfaces*, 2020, **13**, 912–923.
6 B. Sanadgol, S. Holzwarth, P. Uhlig, A. Milano and R. Popovich, *ZTE Commun.*, 2012, **10**, 29–32.
7 U. Illahi, J. Iqbal, M. I. Sulaiman, M. Alam, M. M. Su'ud and M. I. Khattak, *Int. J. Electron. Commun.*, 2020, **126**, 153443.
8 S. U. Anuar, M. H. Jamaluddin, J. Din, K. Kamardin, M. H. Dahri and I. H. Idris, *Int. J. Electron. Commun.*, 2020, **118**, 153172.
9 N. K. Mishra, S. Das and D. K. Vishwakarma, *Int. J. Electron. Commun.*, 2019, **98**, 106–113.
10 X. Wang, X. P. Li, L. H. Cheng, S. Xu, J. S. Sun, J. S. Zhang, X. Z. Zhang, X. T. Yang and B. J. Chen, *RSC Adv.*, 2017, **7**, 23751–23758.
11 R. Haugsrud and T. Norby, *Nat. Mater.*, 2006, **5**, 193–196.
12 R. Abe, M. Higashi, K. Sayama, Y. Abe and H. Sugihara, *J. Phys. Chem. B*, 2006, **110**, 2219–2226.
13 L. H. Brixner, J. F. Whitney, F. C. Zumsteg and G. A. Jones, *Mater. Res. Bull.*, 1977, **12**, 17–25.
14 V. S. Stubican, *J. Am. Ceram. Soc.*, 1964, **47**, 55–58.
15 H. P. Rooksby and E. A. D. White, *Acta Crystallogr.*, 1963, **16**, 888–890.
16 D. W. Kim, D. K. Kwon, S. H. Yoon and K. S. Hong, *J. Am. Ceram. Soc.*, 2006, **89**, 3861–3864.
17 P. Zhang, Z. K. Song, Y. Wang, Y. M. Han, H. L. Dong and L. X. Li, *J. Alloys Compd.*, 2013, **581**, 741–746.
18 T. L. Tang, W. S. Xia, B. Zhang, Y. Wang, M. X. Li and L. W. Shi, *J. Mater. Sci.: Mater. Electron.*, 2019, **30**, 15293–15298.
19 Y. H. Chen, H. Wang, L. X. Pang, H. F. Zhou and X. Yao, *Ferroelectrics*, 2010, **407**, 61–68.
20 Z. K. Song, P. Zhang, Y. Wang and L. X. Li, *J. Alloys Compd.*, 2014, **583**, 546–549.
21 Y. G. Zhao and P. Zhang, *RSC Adv.*, 2015, **5**, 97746–97754.
22 P. Zhang and Y. G. Zhao, *J. Alloys Compd.*, 2016, **654**, 240–245.
23 P. Zhang, Y. Zhao and L. Li, *Phys. Chem. Chem. Phys.*, 2015, **17**, 16692–16698.
24 Y. Zhao and P. Zhang, *Ceram. Int.*, 2018, **44**, 1935–1941.
25 L. X. Pang and D. Zhou, *J. Am. Ceram. Soc.*, 2019, **102**, 2278–2282.
26 M. Xiao, Y. S. Wei, Q. Q. Gu, Z. Q. Zhou and P. Zhang, *J. Alloys Compd.*, 2019, **775**, 168–174.
27 P. Zhang, Y. G. Zhao and X. Y. Wang, *Dalton Trans.*, 2015, **44**, 10932–10938.
28 D. Guo, D. Zhou, W. B. Li, L. X. Pang, Y. Z. Dai and Z. M. Qi, *Inorg. Chem.*, 2017, **56**, 9321–9329.

29 H. C. Yang, S. R. Zhang, H. Y. Yang, Y. Yuan and E. Z. Li, *Ceram. Int.*, 2019, **45**, 16940–16947.
30 H. C. Yang, S. R. Zhang, H. Y. Yang, Y. Yuan and E. Z. Li, *J. Alloys Compd.*, 2019, **787**, 358–366.
31 H. C. Yang, S. R. Zhang, H. Y. Yang, Y. Yuan and E. Z. Li, *Dalton Trans.*, 2018, **47**, 15808–15815.
32 S. J. Kim and E. S. Kim, *Ceram. Int.*, 2009, **35**, 137–141.
33 S. D. Ramarao and V. R. K. Murthy, *Phys. Chem. Chem. Phys.*, 2015, **17**, 12623–12633.
34 W. S. Xia, S. B. Zhang, T. L. Tang, Y. Wang and L. W. Shi, *Phys. B*, 2019, **572**, 148–152.
35 A. T. Alared, *J. Solid State Chem.*, 1985, **59**, 95–102.
36 A. T. Aldred, *Mater. Lett.*, 1983, **1**, 197–199.
37 A. J. Bosman and E. E. Havinga, *Phys. Rev.*, 1963, **129**, 1593–1600.
38 R. D. Shannon, *J. Appl. Phys.*, 1993, **73**, 348–366.
39 C. Nico, M. R. N. Soares, F. M. Costa, T. Monteiro and M. P. F. Graca, *J. Appl. Phys.*, 2016, **120**, 051708.
40 R. D. Shannon, *Acta Crystallogr.*, 1976, **A32**, 751–767.
41 L. Jian, C. M. Huang, G. B. Xu and C. M. Wayman, *Mater. Lett.*, 1994, **21**, 105–110.
42 L. Jian and C. M. Wayman, *J. Am. Ceram. Soc.*, 1996, **79**, 1642–1648.
43 S. Tsunekawa, A. Kasuya and Y. Nishina, *Mat. Sci. Eng.*, 1996, **A217**/**218**, 215–217.
44 Z. L. Zhang, L. Zhou, Y. G. Hu and L. Jiang, *Scr. Mater.*, 2002, **47**, 637–641.
45 K. P. F. Siqueira, R. L. Moreira and A. Dias, *Chem. Mater.*, 2010, **22**, 2668–2674.
46 G. Blasse, *J. Solid State Chem.*, 1973, **7**, 169–171.
47 J. Hou, Q. Chen, C. Gao, R. Dai, J. Zhang, Z. Wang, Z. Zhang and Z. Ding, *J. Rare Earths*, 2014, **32**, 787–791.
48 I. Guedes, Y. Hirano, M. Grimsditch, N. Wakabayashi, C. K. Loong and L. A. Boatner, *J. Appl. Phys.*, 2001, **90**, 1843–1846.
49 C. C. Santos, E. N. Silva, A. P. Ayala, I. Guedes, P. S. Pizani, C. K. Loong and L. A. Boatner, *J. Appl. Phys.*, 2007, **101**, 053511.
50 Q. W. Liao, L. X. Li, X. Ren and X. Ding, *J. Am. Ceram. Soc.*, 2011, **94**, 3237–3240.
51 S. J. Perm, N. M. ALford, A. Templeton, X. R. Wang, M. S. Xu, M. Reece and K. Schrapelt, *J. Am. Ceram. Soc.*, 1997, **80**, 1885–1888.
52 W. Li, L. Fang, Y. H. Sun, Y. Tang, J. W. Chen and C. C. Li, *J. Electron. Mater.*, 2017, **46**, 1956–1962.
53 D. Zhou, L. X. Pang, X. Yao and H. Wang, *Mater. Chem. Phys.*, 2009, **115**, 126–131.
54 E. S. Kim, B. S. Chun, R. Freer and R. J. Cernik, *J. Eur. Ceram. Soc.*, 2010, **30**, 1731–1736.
55 J. W. Chen, L. Fang, J. Li, Y. Tang, K. Cheng and Y. J. Cao, *J. Mater. Sci.: Mater. Electron.*, 2020, **31**, 19180–19187.
56 P. Zhang, Y. G. Zhao and X. Y. Wang, *J. Alloys Compd.*, 2015, **644**, 621–625.
57 Y. G. Zhao and P. Zhang, *J. Mater. Sci.: Mater. Electron.*, 2016, **27**, 2511–2522.
58 L. X. Pang, D. Zhou, Z. M. Qi, W. G. Liu, Z. X. Yue and I. M. Reaney, *J. Mater. Chem. C*, 2017, **5**, 2695–2701.
59 R. S. Yaduvanshi and H. Parthasarathy, *Department of ECE Ambedkar Institute of Advanced Communication Technologies and Research New Delhi*, Delhi India, 2016, pp. 1–11.